SEIS MICA

Supporting Information for Inferring rock strength and fault activation from high-resolution *in-situ* V_p/V_s estimates surrounding induced earthquake clusters

M.P. Roth ◉ * [1], **A. Verdecchia** ◉ [1], **R.M. Harrington** ◉ [1], **Y. Liu** ◉ [2]

[1]Institute of Geology,Mineralogy and Geophysics, Ruhr University Bochum, Bochum, Germany, [2]Department of Earth and Planetary Sciences, McGill University, Montréal, Québec, Canada

Contents of this file

Text S1
Figures S1 - S12
Table S1

Introduction

Supporting Information S1 explains the error assessment for the 3D velocity model using the Gaussian error propagation. Figure S1 shows HF-well information inside the study area. Figure S2 contains an example event pair with 14 common stations, their travel time curves, and the differential arrival-time differences from the catalog, cross-correlation, and picking correction. Figure S3 illustrates the application of the Huber regression ([Huber, 1973](#)). We estimate the quality of linear regression of individual clusters in Figure S4. Figure S5 shows the $\delta v/v$ in percent change over time from ambient noise for stations in networks XL, 1E, and PQ. We use *MSNoise* ([Lecocq et al., 2014](#)) to calculate $\delta v/v$ from the vertical component only. The ambient noise results use data in the frequency range of 0.1 Hz to 1 Hz with instrument response removed. Figure S6 shows the depth distribution of relocated catalog hypocenters used in this study, with an inset showing their relative depths to the horizontal well trajectory (the latter shown with a black line). The color scheme of the inset follows the temporal colorbar indicated in the main text. We highlight well-proximal ($<$200 m) and well-distal ($>$200 m) events in Figure S7. In Figure S8, we calculate mean estimates of the temporal evolution of V_p/V_s-ratio, similar to Figure 5, but with varying numbers of time segments. Figure S9 shows the three additional well pads with $>$ 100,000 observations and their estimated temporal trend in V_p/V_s. The V_p/V_s trend follows the same pattern as the example shown in the main text, namely, an initial phase with slow decreased, followed by a rapid decrease and recovery as the HF-stimulation progresses. We show the iterative estimation of bulk- and shear-modulus according to [Berryman](#) ([1980](#)) in Figure S10. Figure S11 shows the resulting moduli as a function of aspect ratio with respect to theoretical values of Voigt ([Voigt, 1910](#)), Reuss ([Reuss, 1929](#)), and Hashin and Shtrikman ([Hashin and Shtrikman, 1963](#)). Figure S12 shows a simplified version of Figure 6 that depicts the V_p/V_s-ratio color-coded by aspect ratio as a function of fluid fraction. Table S1 provides an overview of the individual *in-situ* V_p/V_s estimates per cluster.

S1 Gaussian error propagation

We use a background reference model to evaluate estimated changes in V_p/V_s-ratios. The reference 3D-model contains both the compressional and shear wave velocities V_p and V_s, respectively, and contains no reported individual uncertainties. In order to consider uncertainties (and their propagation) for measuring and interpreting high-resolution V_p/V_s changes, we derive uncertainties by estimating the Gaussian error propagation (GEP). We calculate the V_p/V_s-ratio in an example we refer to as R, by the following:

$$R = \frac{V_p}{V_s}.$$

(S1)

---

*Corresponding author: marco.roth@rub.de

37 Following GEP, the resulting uncertainty, ΔR, is described by

$$\Delta R = \sqrt{\sum_{i=1}^{n}\left(\frac{\partial R}{\partial x_i}\cdot\Delta x_i\right)^2} = \sqrt{\left(\frac{1}{V_s}\Delta V_p\right)^2 + \left(-\frac{V_p}{V_s^2}\Delta V_s\right)^2}, \qquad \text{(S2)}$$

38 where ΔV_p and ΔV_s are the individual errors of V_p and V_s, respectively, and $R(V_p, V_s)$. Here, we assume an error of
39 1.5%, i.e., $\Delta V_p = 0.015 V_p$ and $\Delta V_s = 0.015 V_s$. Substituting leads to

$$\Delta R = \sqrt{\left(\frac{1}{V_s}\cdot 0.015 V_p\right)^2 + \left(-\frac{V_p}{V_s^2}\cdot 0.015 V_s\right)^2} \approx 0.0212\,\frac{V_p}{V_s}, \qquad \text{(S3)}$$

40 corresponding to an approximate error of 2.12% for each grid point of V_p/V_s.
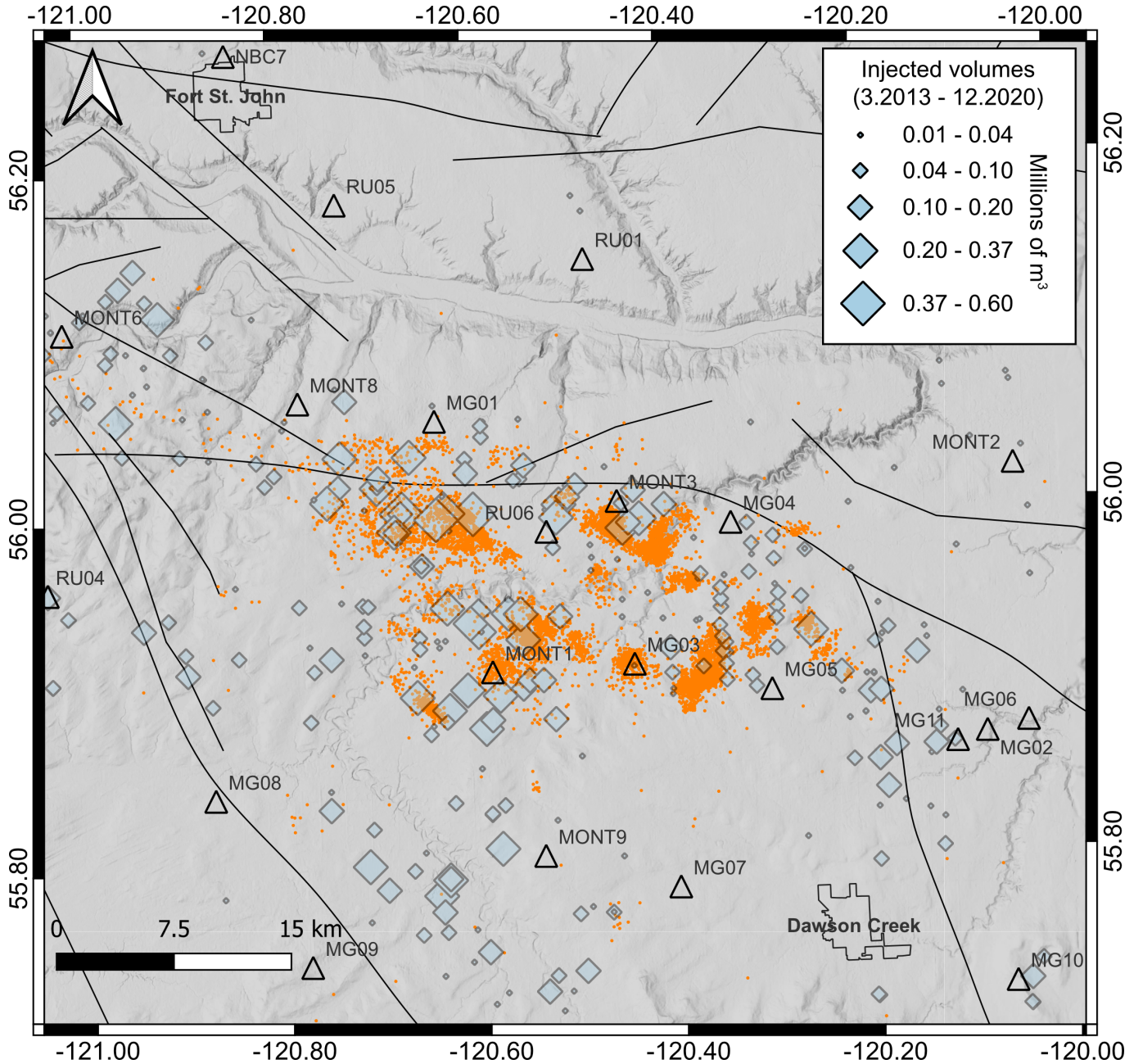

Figure S1 Overview of the Kiskatinaw area, extending between Fort St. John (NW) and Dawson Creek (SE). Orange dots show locations of 8,731 individual earthquakes between 12 July 2017 and 31 December 2020. Diamonds show the locations of HF wells, scaled by injected volume (cumulative between March 2013 and December 2020). Triangles denote seismic stations from networks XL, 1E, and PQ. Black lines are mapped fault traces.
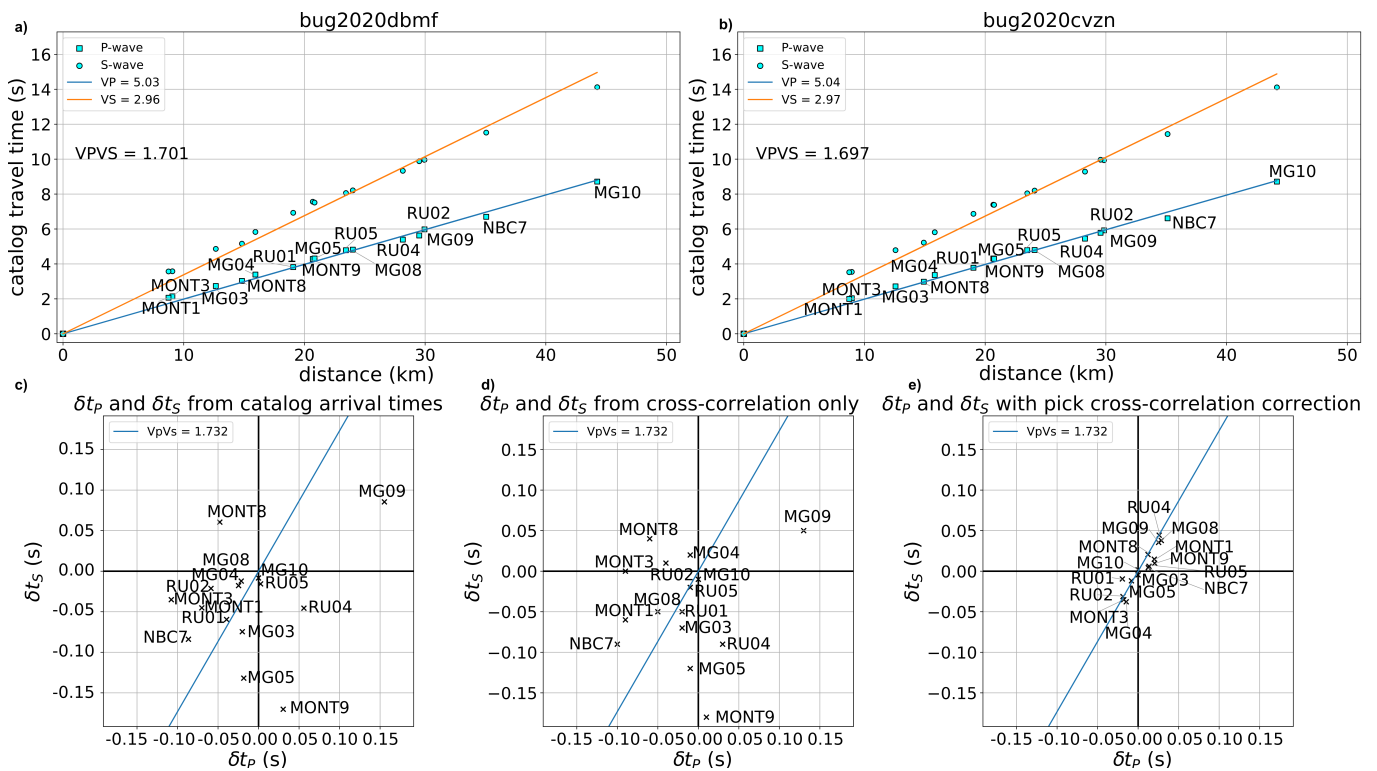
Figure S2 One event pair from one cluster. a) and b) show travel time curves for P-waves (squares and blue lines) and S-waves (circles and orange lines) for an event pair. a) is a ML 2.8 on 2020-02-13T11:55:14.262, b) a co-located ML 2.7 on 2020-02-10T11:48:40.394. c)-e) show the differential arrival time differences for cataloged arrival times, followed by the cross-correlation, and their combination as picking correction, respectively.
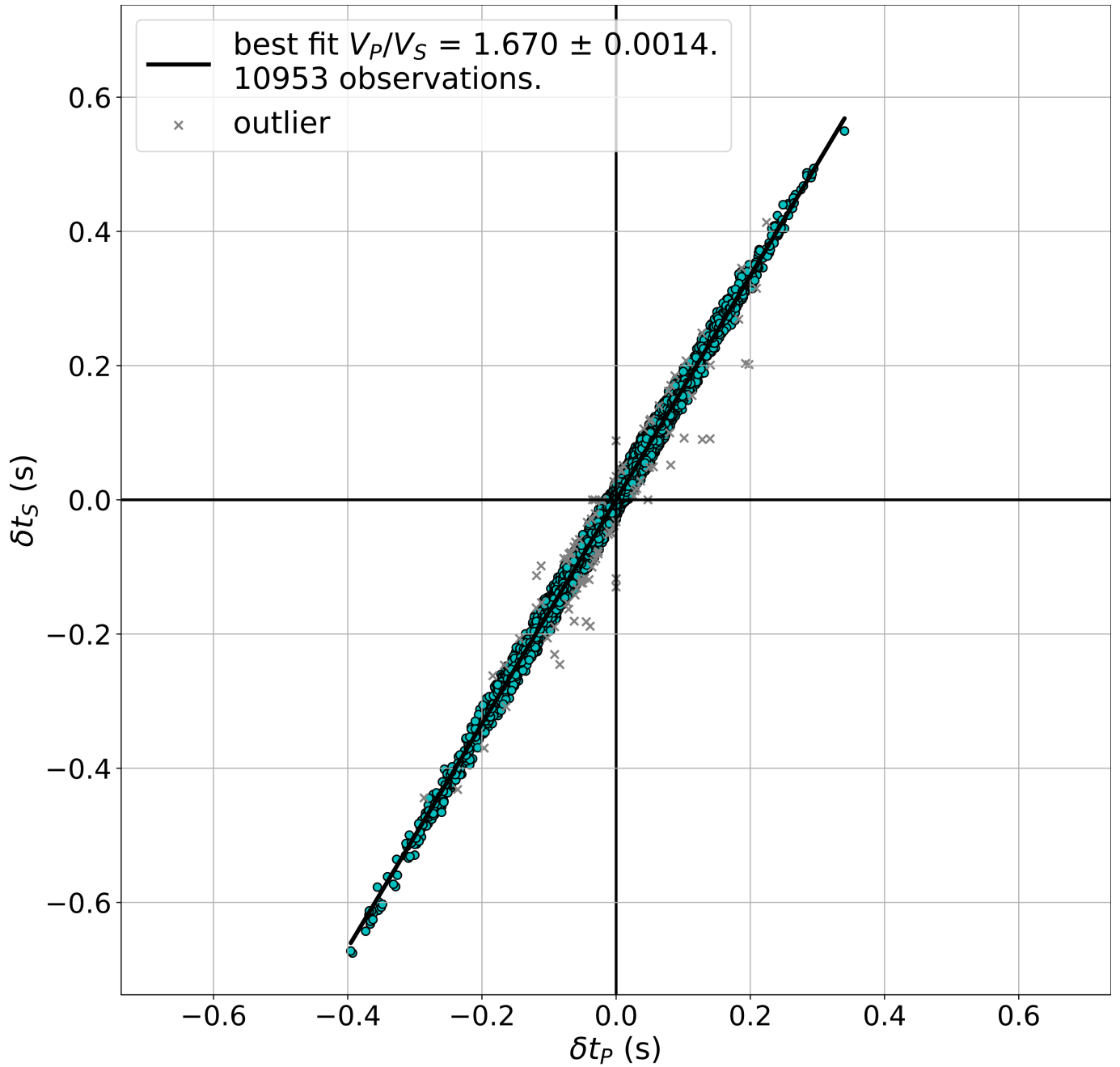
Figure S3 V_p/V_s-ratio regression (black line) for a representative cluster. Each circle denotes the δt s vs. δt p differential body-wave travel-time differences for one event pair recorded on an individual station. Crosses denote outliers excluded from the Huber regression.
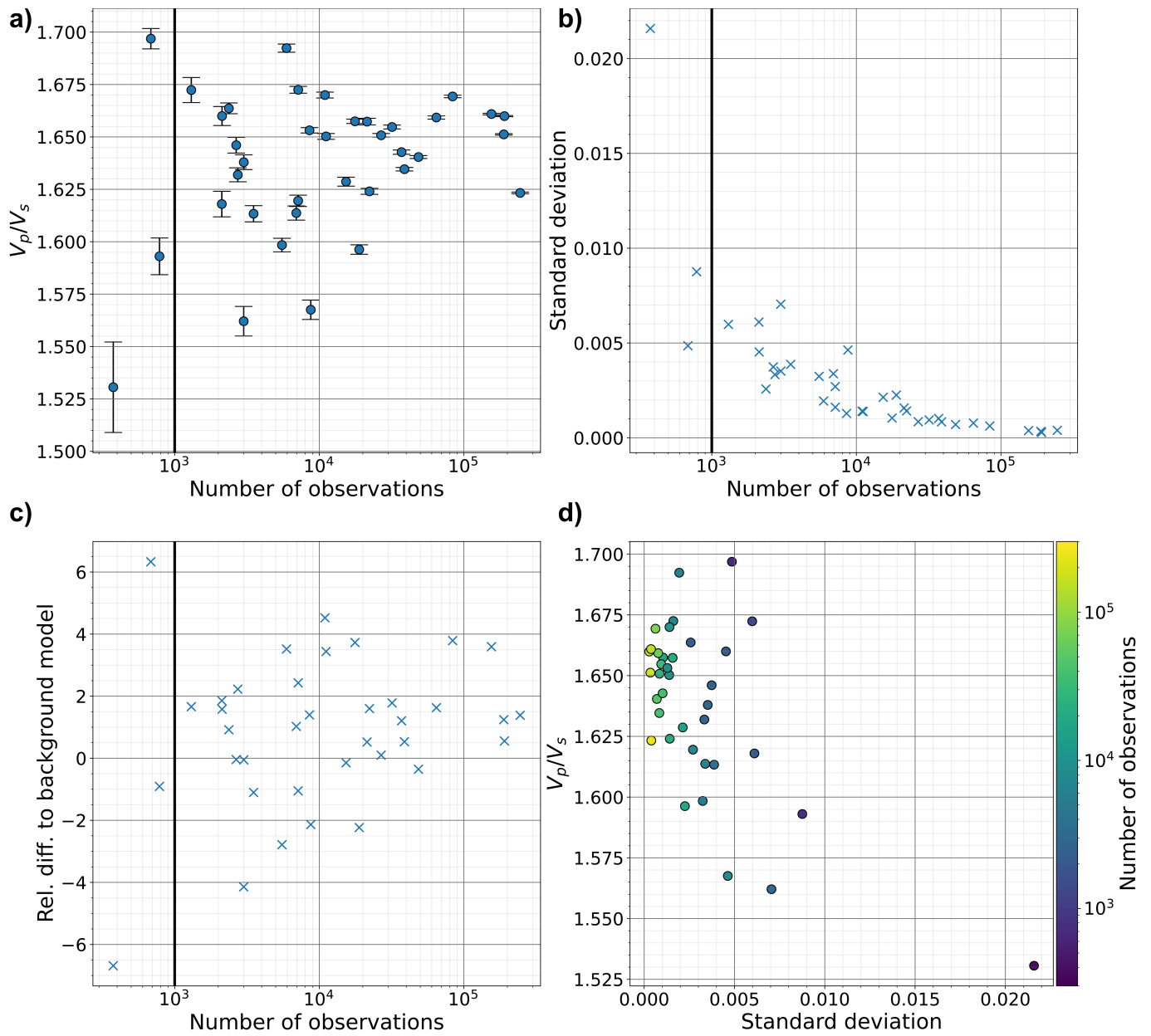
Figure S4 Impact of cluster size on V_p/V_s-ratio. a) V_p/V_s vs. the number of observations per cluster, b) standard deviation following linear regression vs. the number of events per cluster, c) relative level of change between *in-situ* estimate and background raster value vs. the number of observations, and d) V_p/V_s-ratio vs. standard deviation, color-coded by the number of observations. The horizontal black line marks the threshold of 1000 events per cluster used in this study.
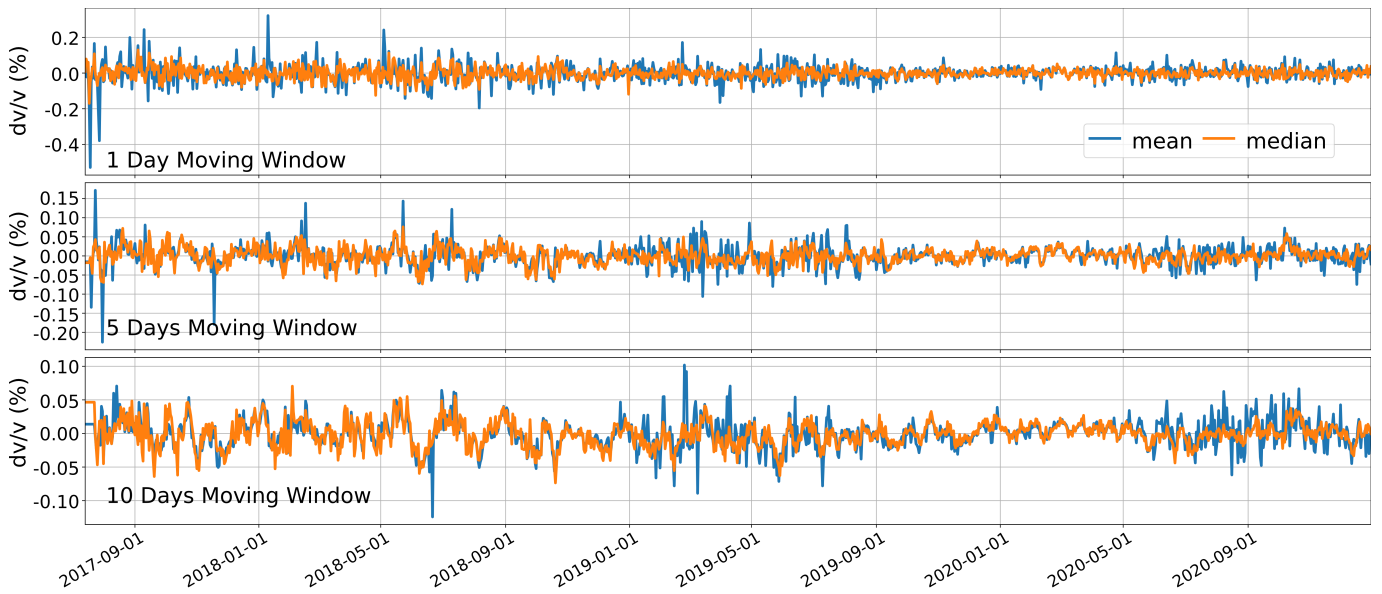
Figure S5   Rock medium velocity change on the vertical component in a frequency range of 0.1 Hz to 1 Hz estimated from ambient noise of stations in networks XL, 1E, and PQ (Lecocq et al., 2014). The panels show 1-day, 5-day, and 10-day time windows from top to bottom, respectively. The blue and orange lines shows the mean and median estimates per time window, respectively.
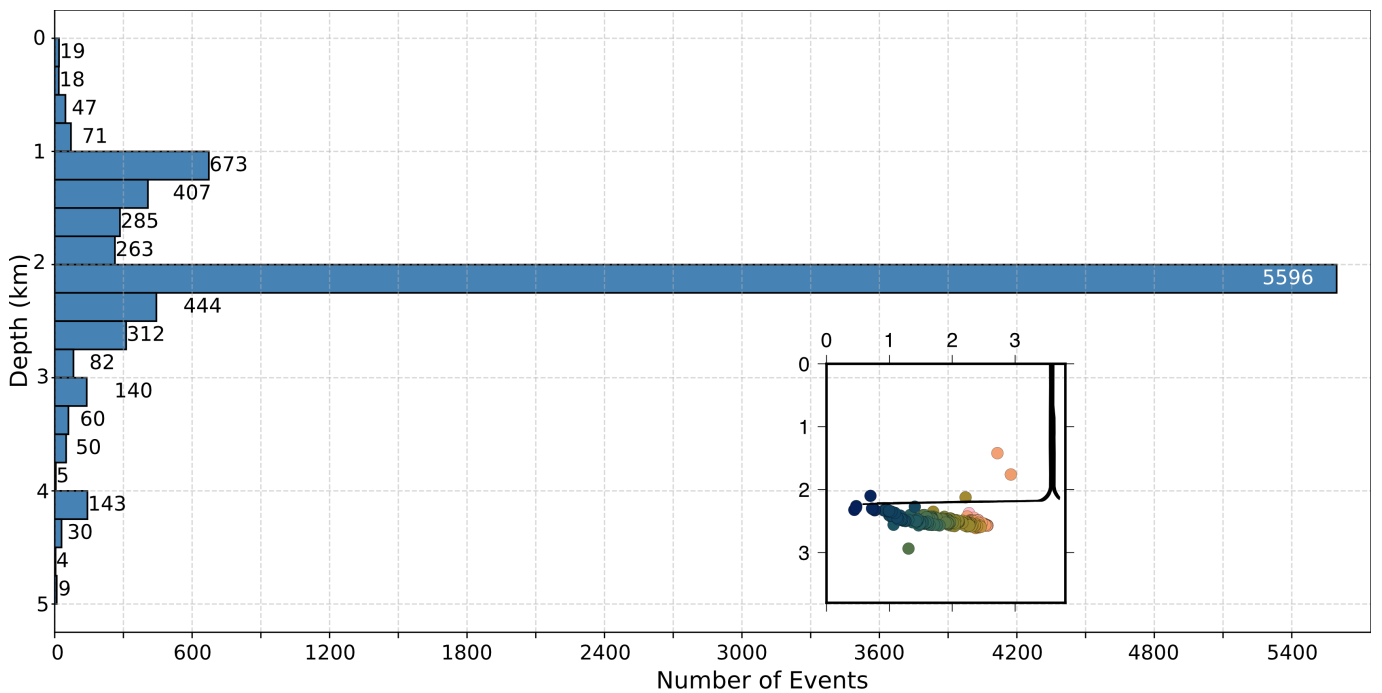

Figure S6   Depth distribution of all events in the study area. The inset map shows the well pad from Figure 4 as an example.
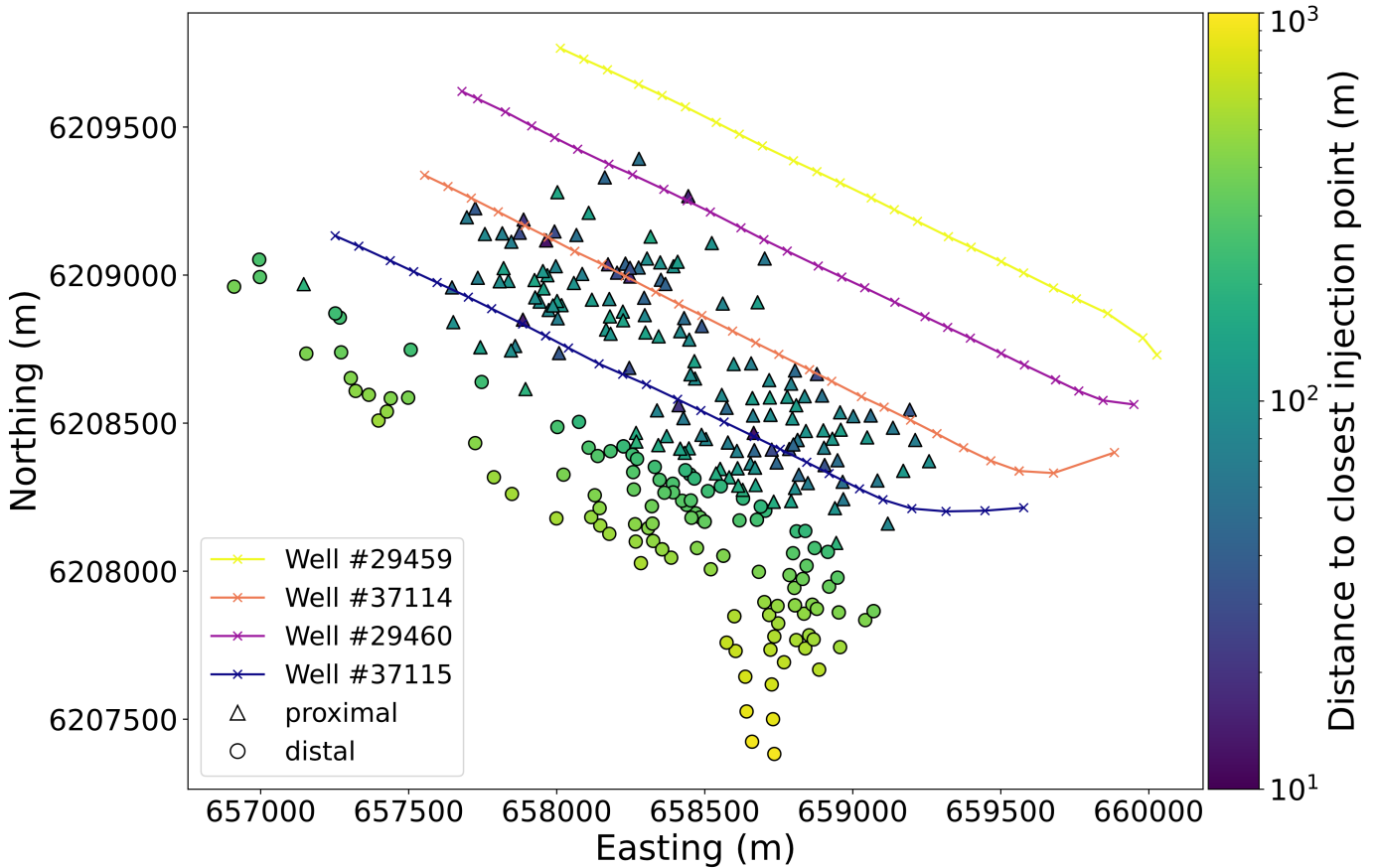
Figure S7   Map view of the western horizontal well trajectories shown in the map in Figure 4. Color denotes the well number documented in the BCOGC database. Each cross marks an HF stage. Triangles show events located <200 m to the closest HF stage, circles are events located >200 m to the nearest stage. The color bar shows the epicentral distance to the nearest stage in meters.
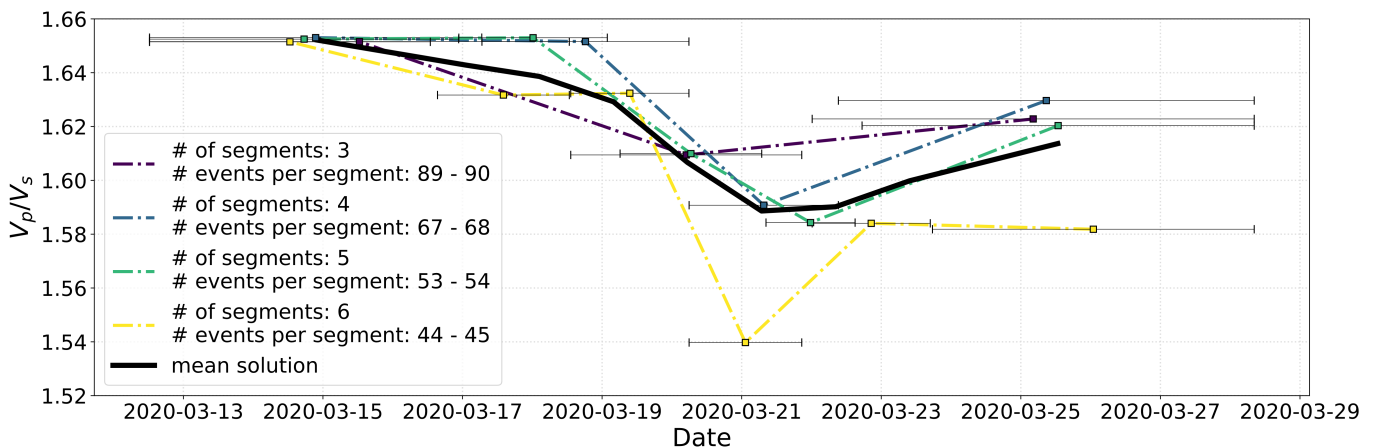

Figure S8   Temporal segmentation of the data set used in Figure 5. Each colored dashed line represents all events within the northwestern cluster in Figure 4 (maroon box), here split into a range of 3-6 of segments to check for consistency in the temporal trend of estimates. For example, the chronological segmentation of all events into 3 segments results in 89 to 90 events per segment, while 6 segments result in 44 to 45 events per segment. Horizontal bars show the time-window length over which each segment extends. The thick black line represents the interpolated mean estimate of all segments after re-sampling each individual trend to 11 data points.
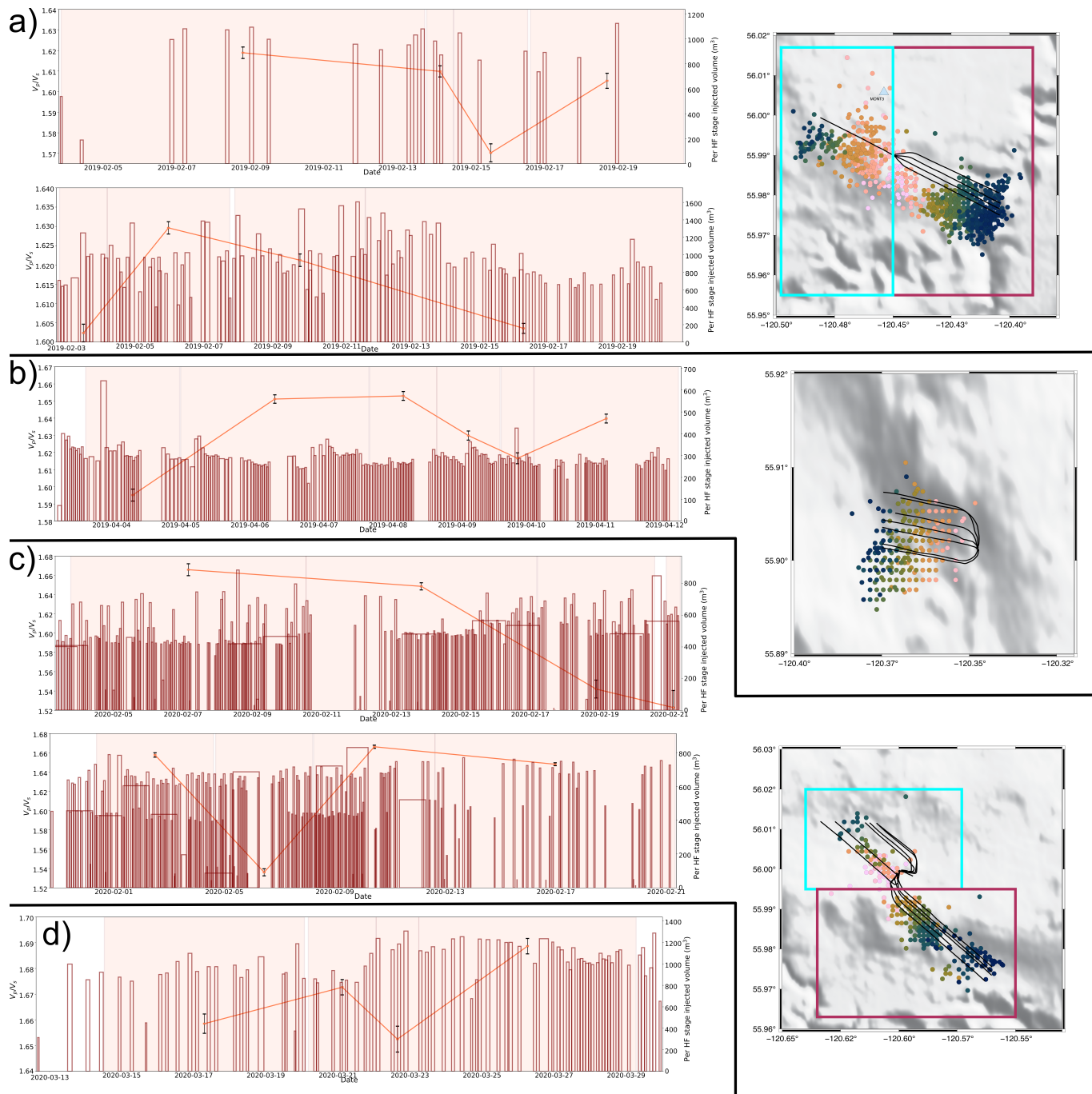
Figure S9   Additional examples of three injection sites with >100,000 observations ((a) - (c)). Histogram shows the temporal trend of V_p/V_s, analogous to Figure 5. (d) shows the eastern section of the well pad from Figure 4.
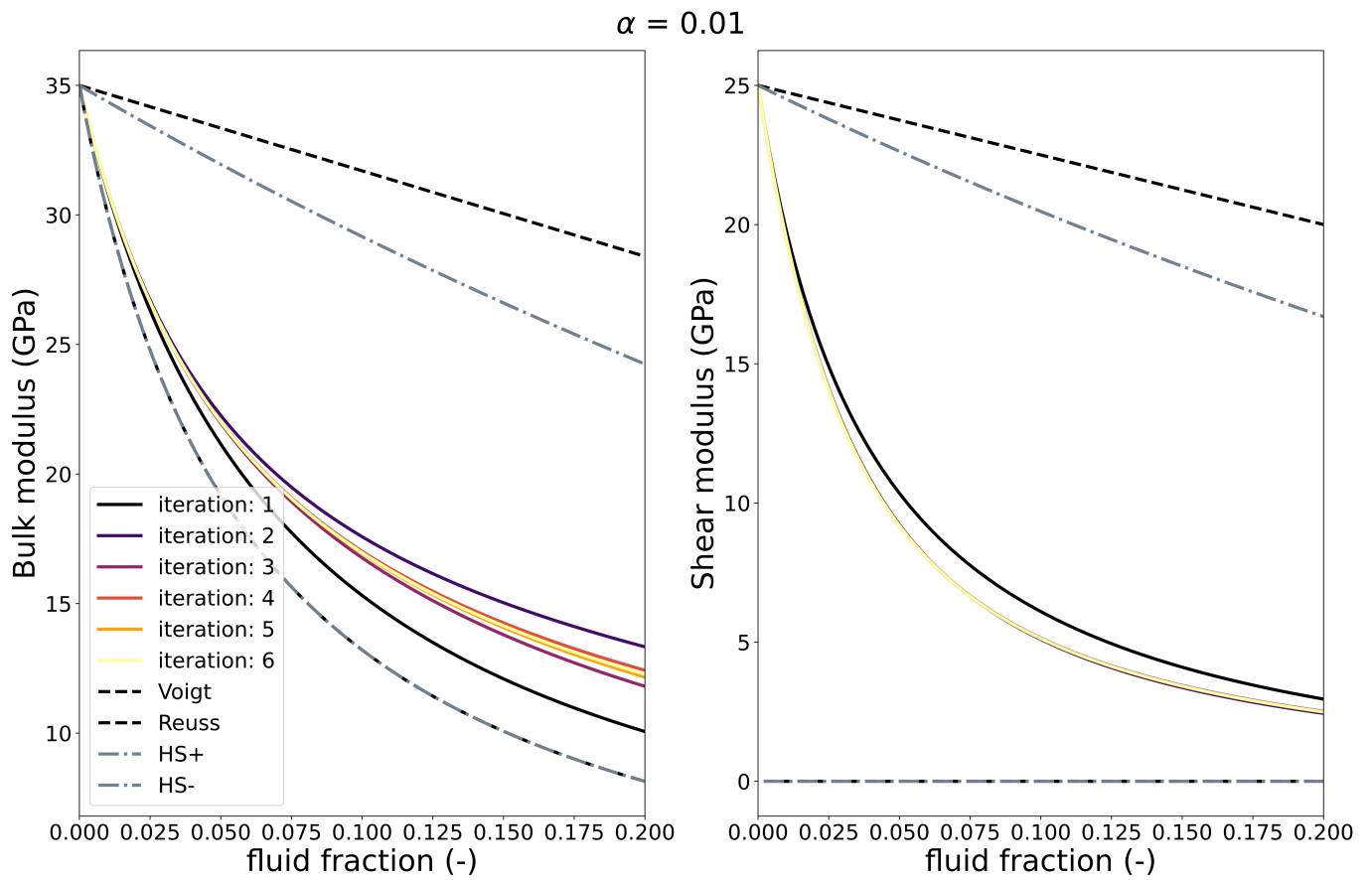
Figure S10   Example estimates of bulk and shear modulus as a function of fluid content for a fixed aspect ratio. We apply the self-consistent models (Berryman, 1980) for a penny-shaped crack of aspect ratio $\alpha = 0.01$. Colors show the nth iteration according to the numerical solution. Theoretical boundaries following Voigt (1910); Reuss (1929); Hashin and Shtrikman (1963).
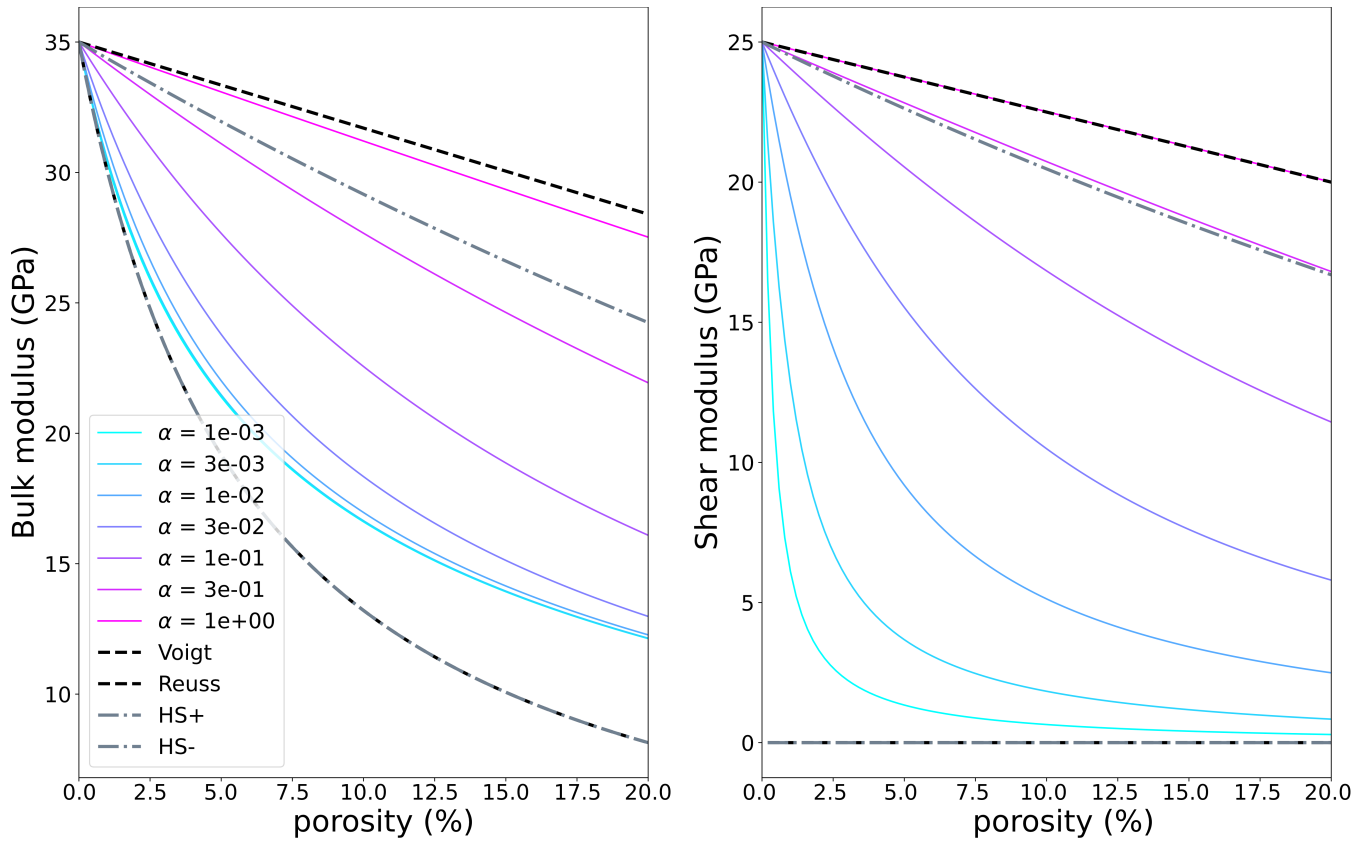
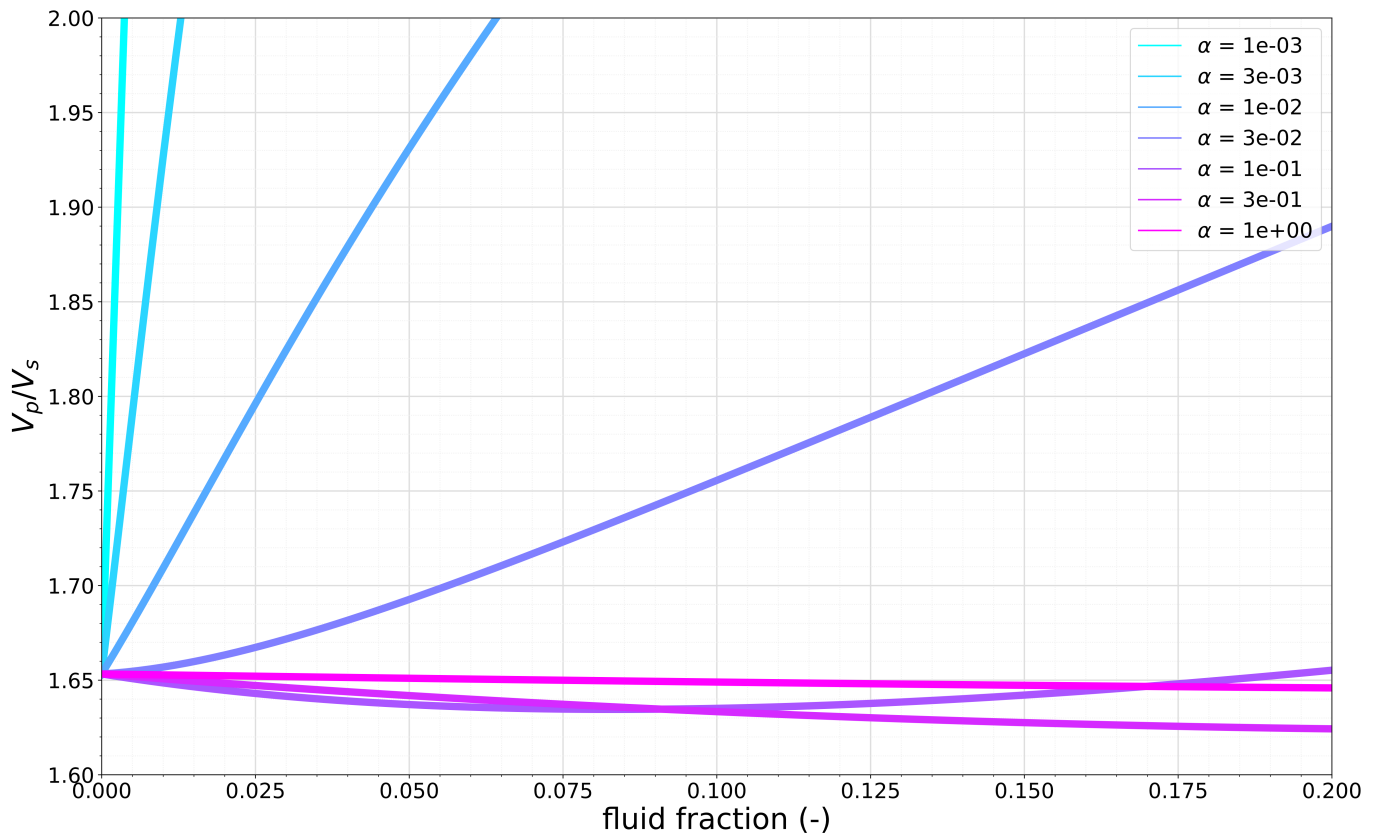**Figure S11** Bulk and shear moduli as a function of fluid content for different aspect ratios α, where we apply six iterations for each. Theoretical boundaries following Voigt (1910); Reuss (1929); Hashin and Shtrikman (1963). Stiff pore geometries (i.e., α approaching unity), will cause the model to exaggerate the HS boundaries, which do not consider pore geometry.

Figure S12 V_p/V_s-ratio as a function of fluid fraction, colored by aspect ratio α.

V_p/V_s	standard error	# of observations	background value	relative deviation (%)
1.623	0.00039	245286	1.601	1.38
1.660	0.00028	190960	1.651	0.56
1.651	0.00034	189036	1.631	1.24
1.661	0.00038	155296	1.603	3.59
1.669	0.00063	83681	1.608	3.79
1.659	0.00078	64562	1.633	1.63
1.640	0.00070	48550	1.646	-0.35
1.635	0.00084	38839	1.626	0.53
1.643	0.00102	37091	1.623	1.21
1.655	0.00094	31875	1.626	1.78
1.651	0.00085	26798	1.649	0.10
1.624	0.00142	22246	1.598	1.60
1.657	0.00158	21393	1.649	0.52
1.596	0.00226	18895	1.633	-2.23
1.657	0.00104	17666	1.598	3.73
1.629	0.00214	15329	1.631	-0.15
1.650	0.00139	11141	1.595	3.44
1.670	0.00140	10953	1.598	4.52
1.568	0.00463	8739	1.602	-2.14
1.653	0.00128	8556	1.630	1.40
1.672	0.00161	7152	1.633	2.43
1.620	0.00270	7144	1.637	-1.05
1.614	0.00338	6938	1.597	1.03
1.692	0.00194	5934	1.635	3.52
1.598	0.00324	5520	1.644	-2.79
1.613	0.00387	3513	1.631	-1.10
1.638	0.00352	3006	1.639	-0.05
1.562	0.00705	3002	1.630	-4.14
1.632	0.00333	2733	1.596	2.23
1.646	0.00374	2664	1.647	-0.04
1.664	0.00258	2370	1.649	0.92
1.660	0.00453	2126	1.634	1.58
1.618	0.00610	2118	1.588	1.86
1.672	0.00598	1303	1.645	1.66
1.593	0.00876	785	1.608	-0.91
1.697	0.00486	684	1.596	6.33
1.531	0.02159	376	1.640	-6.69

Table S1 Per-cluster estimates of *in-situ* V_p/V_s-ratio with standard deviation following linear regression, number of observations per data set, the background raster value of the 3D velocity model at the cluster centroid location, and the relative deviation of *in-situ* estimate to the background value. We only include clusters with >300 observations, as smaller clusters do not produce robust fits.

References

Berryman, J. G. Long-wavelength propagation in composite elastic media II. Ellipsoidal inclusions. *The Journal of the Acoustical Society of America*, 68(6):1820–1831, 1980. doi: 10.1121/1.385172.

Hashin, Z. and Shtrikman, S. A variational approach to the theory of the elastic behaviour of multiphase materials. *Journal of the Mechanics and Physics of Solids*, 11(2):127–140, 1963. doi: 10.1016/0022-5096(63)90060-7.

Huber, P. J. Robust regression: Asymptotics, conjectures and Monte Carlo. *The Annals of Statistics*, 1(5):799–821, 1973.

Lecocq, T., Caudron, C., and Brenguier, F. MSNoise, a Python package for monitoring seismic velocity changes using ambient seismic noise. *Seismological Research Letters*, 85(3):715–726, 2014. doi: 10.1785/0220130073.

Reuss, A. Calculation of the flow limits of mixed crystals on the basis of the plasticity of monocrystals. *Z. Angew. Math. Mech*, 9:49–58, 1929.

Voigt, W. *Lehrbuch der Kristallphysik:(mit Ausschluss der Kristalloptik)*, volume 34. BG Teubner, 1910.